NANOSCALE ELASTIC PROPERTIES OF DRY AND WET SMECTITE

JUNFANG ZHANG, MARINA PERVUKHINA, AND MICHAEL B. CLENNELL

CSIRO Energy, 26 Dick Perry Ave, Kensington, WA 6151, Australia

Abstract—The nanoscale elastic properties of moist clay minerals are not sufficiently understood. The aim of the present study was to understand the fundamental mechanism for the effects of water and pore size on clay mineral (K^+-smectite) elastic properties using the General Utility Lattice Program (GULP) with the minimum energy configurations obtained from molecular dynamics (MD) simulations. The simulation results were compared to an ideal configuration with transversely isotropic symmetry and were found to be reasonably close. The pressures computed from the MD simulations indicated that the changes due to water in comparison to the dry state varied with the water content and pore size. For pore sizes of around 0.8−1.0 nm, the system goes through a process where the normal pressure is decreased and reaches a minimum as the water content is increased. The minimum normal pressure occurs at water contents of 8 wt.% and 15 wt.% for pore sizes of around 0.8 nm and 1 nm, respectively. Further analyses of the interaction energies between water and K^+-smectite and between water and water revealed that the minimum normal pressure corresponded to the maximum rate of slope change of the interaction energies (the second derivative of the interaction energies with respect to the water content). The results indicated that in the presence of water the in-plane stiffness parameters were more correlated to the pressure change that resulted from the interplay between the interactions of water with K^+-smectite and the interactions of water with water rather than the water content. The in-plane stiffness parameters were much higher than the out-of-plane parameters. Elastic wave velocities for the P and S waves (V_P and V_S) in the dry K^+-smectite with a pore size of ~1 nm were calculated to be 7.5 and 4.1 km/s, respectively. The P and S wave velocity ratio is key in the interpretation of seismic behavior and revealed that $V_P/V_S = 1.64−1.83$, which were values in favorable agreement with the experimental data. The results might offer insight into seismic research to predict the mechanical properties of minerals that are difficult to obtain experimentally and can provide complimentary information to interpret seismic surveys that can assist gas and oil exploration.

Key Words—Elastic Properties, Molecular Dynamics Simulation, Normal Pressure, P-wave and S-wave Velocities, Smectite.

INTRODUCTION

Smectite is one of the most common clay minerals in shale source rocks, and smectite behavior under different water contents is of practical importance in petroleum exploration and geophysics (Hornby *et al.*, 1994; Lein *et al.*, 2000; Bayuk *et al.*, 2007; Chalmers and Bustin, 2008; Witteveen *et al.*, 2013; Zou *et al.*, 2015). A knowledge of clay elastic properties is essential to understand seismogenic zones and to interpret and model the seismic response of clay-bearing geological formations. The elastic properties of moist clay minerals on the nanoscale, however, are still not sufficiently understood. Elastic properties of clays have been studied theoretically and experimentally (Prasad *et al.*, 2002; Vanorio *et al.*, 2003; Khazanehdari and McCann, 2005; Schon *et al.*, 2006; Renner *et al.*, 2007; Wang *et al.*, 2009; Kitamura *et al.*, 2010; Knuth *et al.*, 2013; Carpenter *et al.*, 2014; Sarout *et al.*, 2014; Schumann *et al.*, 2014; Cook *et al.*, 2015; El Husseiny and Vanorio, 2015; Hulan *et al.*, 2015; Jankula *et al.*, 2015; Jeppson and Tobin, 2015; Kleipool *et al.*, 2015; Woodruff *et al.*,

2015; Hulan *et al.*, 2016). Recently the elastic properties of kaolinite were determined using density functional theory (DFT) calculations (Sato *et al.*, 2005) and MD simulations based on the energy minimization technique (Benazzouz and Zaoui, 2012). The high-energy synchrotron X-ray diffraction method has been used to study the elastic anisotropy of illite-rich shale (Wenk *et al.*, 2007).

Molecular computer simulations have provided critical insight to understand the fundamental mechanisms that control many physical, chemical, and thermodynamic properties of clay minerals (Ebrahimi *et al.*, 2016; Escamilla-Roa *et al.*, 2016; Ferrage, 2016; Kalinichev *et al.*, 2016). Molecular simulation studies and mathematical modelling have been reported for hydrated clays (Skipper *et al.*, 1991a, 1991b; Boek *et al.*, 1995; Smith, 1998; Young and Smith, 2000; Zhou *et al.*, 2016) and for clay elastic properties (Carcione, 2000; Chesnokov *et al.*, 2009; Hantal *et al.*, 2014). Isothermal, isobaric interlayer water adsorption by Wyoming Na-montmorillonite was investigated using MD with the CLAYFF force field (Ebrahimi *et al.*, 2012). The effects of clay mineral adsorbed water and the interlayer distance on methane (CH_4) adsorption (Liu *et al.*, 2013) and the importance of shale composition and pore structure on the gas storage potential of shale gas reservoirs (Ross and Bustin, 2009) have been explored

* E-mail address of corresponding author:
Junfang.Zhang@csiro.au

using static volumetric techniques with an automatic Sieverts' apparatus and Hg porosimetry analysis methods. Simulating clay elastic properties is challenging, however, because significant differences exist between the simulation methods. The magnitude of the in-plane stiffness parameters measured by Hantal *et al.* (2014) were about 45–411% higher than the values measured by Militzer *et al.* (2011) and 40–80% higher than the values reported by Sato *et al.* (2005) for different clay minerals. Hantal *et al.* (2014) carried out their MD simulations using the LAMMPS simulation package at a constant volume and a temperature of 300 K and analyzed the elasticity tensor of illite using the GULP 3.1 program package, while Militzer *et al.* (2011) and Sato *et al.* (2005) derived their elastic properties using first-principles calculations based on density functional theory (DFT). Mazo *et al.* (2008), Ebrahimi *et al.* (2012), Carrier *et al.* (2014), and Zhang *et al.* (2017) investigated the elastic properties of hydrated montmorillonites. They reported in-plane stiffness values of C_{11} (186.8–227.6 GPa), C_{22} (177.2–263.2 GPa), C_{12} (83.9–115.2 GPa), and C_{66} (45.5–68.0 GPa). They reported out-of-plane stiffness magnitudes of C_{13} (3.4–17.0 GPa), C_{33} (7.8–80.0 GPa), C_{44} (1.6–21.0 GPa), and C_{55} (0.3–22 GPa). The variation of the in-plane and out-of-plane stiffness values was around 18–34% and 80–99%, respectively. The variation in the out-of-plane stiffness values was more significant than the in-plane values.

In the present study, the aim was to understand the pressure behavior mechanism of wet clay minerals (K^+-smectite) by investigating water - K^+-smectite and water - water interactions and the correlations with changes in pressure using the dry clay mineral as reference. Elastic constants for K^+-smectite with various pore sizes and water contents (the percent water content was defined as the ratio of water mass to the total sample mass times 100 (*i.e.* 100 × (water mass/total mass))) were simulated using combined MD simulation methods and the GULP program to examine the effect of water content on the elastic properties and demonstrate the potential use of this modeling method for characterizing rock properties from a molecular perspective.

SIMULATION MODELING

Smectite

The system examined in the present study consisted of K^+-smectite and water (H_2O) (Figure 1a). Smectite is a 2:1 clay mineral, which is a typical constituent of sedimentary rocks, especially shales. In 2:1 clay minerals, an octahedral sheet is sandwiched between two tetrahedral sheets. In this study, the smectite mineral formula composition of $K_x[Si_{(8-x)}Al_x](Al_4)O_{20}(OH)_4$, where $x = 1$ was used, which has an overall layer charge of -1.0 e per smectite unit cell (*i.e.* a beidellic smectite, see Brindley, 1980). Pyrophyllite, smectite (*e.g.* montmorillonite and beidellite), and illite are structurally comparable 2:1 layer silicates. Pyrophyllite has a layer charge of 0, smectites have a layer charge of -0.4 to -1.2, and illites have a layer charge of -1.2 to -1.8 e per O_{20} unit cell (Bailey, 1980; Gualtieri, 2008; Liu, 2013). Of the pyrophyllite, smectite, and illite 2:1 layer silicates, only the smectites are expandable.

The pyrophyllite unit cell parameters: $a = 0.516$ nm, $b = 0.896$ nm, $c = 0.935$ nm, α 91.03º, $\beta = 100.37º$, $\gamma = 89.75º$ (Wardle and Brindley, 1972; Sainz-Diaz *et al.*, 2001; Sainz-Diaz *et al.*, 2003) were used for smectite. The smectite simulation cell contained 45 smectite unit cells ($5 \times 3 \times 3$), which resulted in a 2.58 nm × 2.69 nm patch of clay with basal spacings that ranged from 0.93 nm to 1.66 nm to represent clay nanopores with
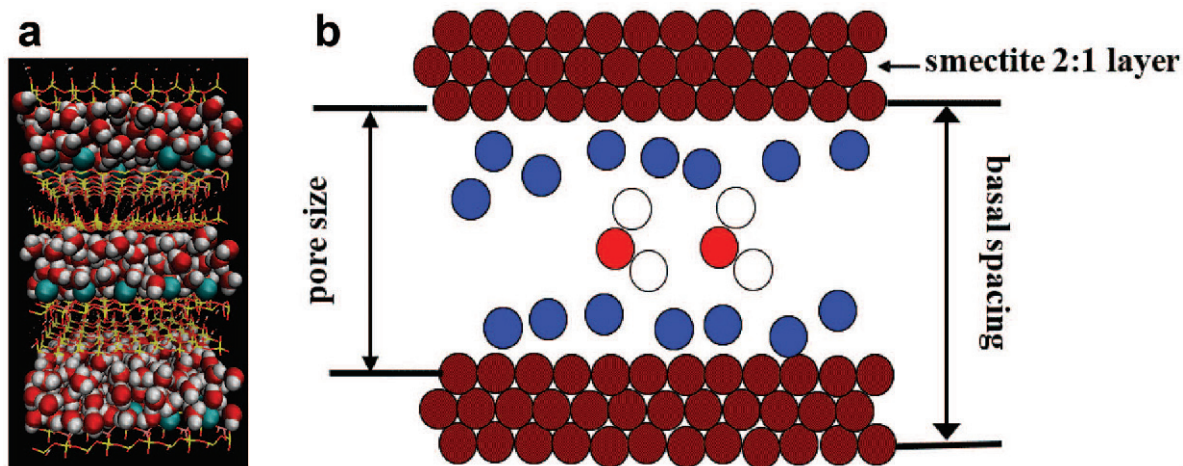

Figure 1. (a) Snapshot of the smectite, water, and interlayer cation (K^+) system. Water molecules are represented by V-shaped molecules that include one oxygen and two hydrogens. The interlayer cations are represented by spheres and the smectite interlayer structure. (b) Schematic illustration of basal spacing and pore size.

different pore sizes. The pore size was defined as the distance between the centers of the interlayer oxygen atom planes (Figure 1b).

In the simulation cell, isomorphic substitutions were made by replacing one Si atom with one Al atom in every replicated clay unit cell (Chen et al., 2016; Zhang et al., 2016). Potassium ions (K^+) were distributed randomly in the clay interlayer space (pore space) to balance the electrostatic charges induced by the isomorphic substitutions in the layers.

Simulation details

In the MD simulation, the smectite layers were considered to be rigid. The two clay layers form slit-shaped nanopores (*i.e.* interlayers) with various pore sizes that depend on basal spacing. Potassium ions and water were movable within the pore. Initially, water molecules were randomly placed between the smectite layers and the number of water molecules in the system was predetermined by the water contents. The smectite was modeled using the CLAYFF force field because Cygan et al. (2004) demonstrated that the force field was suitable for the simulation of hydrated and multicomponent mineral systems and the interfaces with aqueous solutions. Water molecules were simulated using the simple point charge (SPC) water model (Berendsen et al., 1987). Detailed parameter sets for smectite can be found in Cygan et al. (2004). The non-bonded interactions were the sum of van der Waals and electrostatic (Coulomb) interactions between all pairs of atoms. Pair-wise additive Lennard-Jones (LJ) 12-6 potentials were used to describe the potential energies of interaction between two non-bonding atoms based on the separation distance

$$u(r)_{ij} = \begin{cases} 4\varepsilon_{ij}\left[\left(\dfrac{\sigma_{ij}}{r_{ij}}\right)^{12} - \left(\dfrac{\sigma_{ij}}{r_{ij}}\right)^{6}\right] & \text{for } (r_{ij} \leq r_{\text{cut}}) \\ 0 & \text{for } (r_{ij} > r_{\text{cut}}) \end{cases} \quad (1)$$

where r_{ij}, ε_{ij}, and σ_{ij} were the separation distance, LJ well depth, and LJ radius, respectively, for the pair of atoms i and j. The cutoff distance r_{cut} in the LJ potentials was introduced to reduce the computational effort and interactions longer than this distance were omitted from the energy and force computations because beyond this distance the potentials and forces become negligible. Cross interactions between unlike atoms i and j were calculated using the Lorentz-Berthelot combining rules given below:

$$\sigma_{ij} = \frac{1}{2}(\sigma_{ii} + \sigma_{jj}) \quad (2)$$

$$\varepsilon_{ij} = \sqrt{\varepsilon_{ii}\varepsilon_{jj}} \quad (3)$$

A truncated and shifted potential with a cutoff radius of 1.2 nm was used. The Coulomb interactions in the system were calculated using the Ewald summation for periodic systems (Essmann, 1995).

The MD simulation was performed in the NVT ensemble, where the number of water molecules, volume, and temperature were maintained constant. Pore sizes of 0.45 nm to 1 nm with water contents that varied from 0 to 25 wt.% were simulated at 353 K. The simulations modeled a typical experiment using a surface force apparatus to measure the force, which for example is the force between two mica layers immersed in water (Horn, 1990). The effect of the water content on the elastic properties was investigated. To focus on the effects caused by clay interactions with water and K^+, the contribution of the direct interactions between the clay layers was subtracted from the pressure.

In the MD simulation, the temperature was fixed using a Berendsen thermostat (Berendsen et al., 1984) and periodic boundary conditions were applied in three directions. The equations of motion were integrated using a time step of 0.001 ps and each MD run was done in two steps. For every system, the simulation was equilibrated for at least 10^6 time steps followed by at least 5×10^6 production run (5 ns) steps. The evolution of total energy and average pressure over the simulation time was monitored to check for equilibration conditions.

In this study, MD simulations were carried out using the GROMACS (Van der Spoel et al., 2005) simulation package and the elastic properties were calculated using the General Utility Lattice Program (GULP) (Gale, 1997) to minimize the energy of the configuration obtained from the MD simulations. In Voigt notation, the fourth-order elasticity tensor can be represented using a symmetrical matrix with components C_{ij}, which are the second derivatives of the energy with respect to the strains:

$$C_{ij} = \frac{1}{V}\frac{\partial^2 U}{\partial \varepsilon_i \partial \varepsilon_j} \quad (4)$$

where V is the volume of the simulation cell, U is the potential energy, and ε_i and ε_j represent the components of the second-order strain tensor in Voigt notation.

RESULTS AND DISCUSSION

Pressure

For a basal spacing of 1.11 nm, it was difficult to reach a water content of more than 10 wt.% because of the limited pore space (Figure 2a). The zoomed-in plot of Figure 2a in the range −0.2 to 0.6 GPa (Figure 2b) revealed that at basal spacings of 1.47 and 1.66 nm (which correspond to pore sizes of around 0.8 and 1 nm) a minimum in the normal pressure was reached before the normal pressure consistently increased at water contents of around 8 wt.% and 15 wt.%, respectively. A negative P_{zz} value suggests that the two smectite sheets are being pulled towards each other. Analysis of the P_{xx} component (Figure 2c) indicated that a negative pressure was also present in this dimension as P_{zz} and
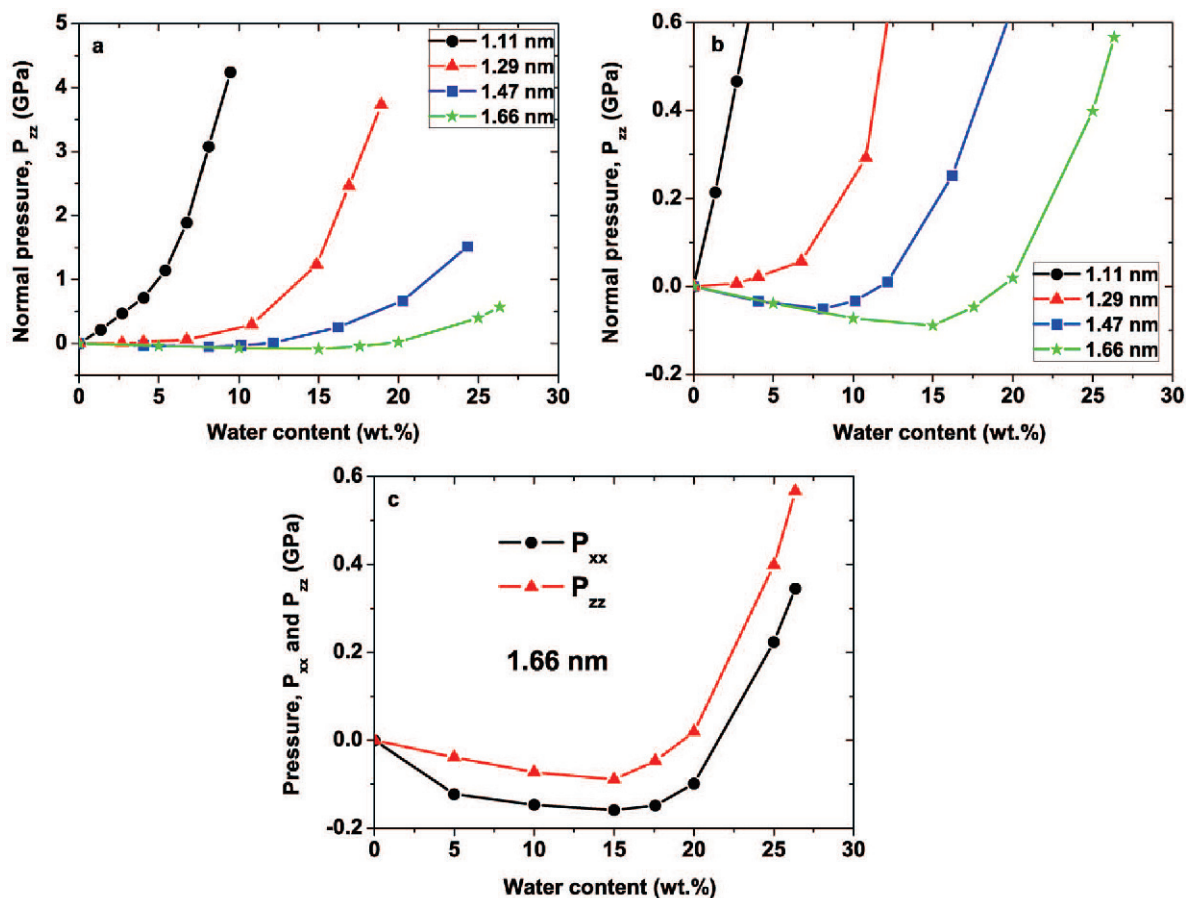
Figure 2. (a) Normal pressure, P_{zz}, with reference to the dry state for the K^+-smectite with various basal spacings and water contents; (b) the same plot as (a) for a $-0.2-0.6$ GPa normal pressure range; (c) pressure components P_{xx} and P_{zz} with reference to the dry state for K^+-smectite with a 1.66 nm basal spacing and various water contents.

might provide a "suction" force. The minimum pressure (Figures 2b and 2c) corresponded to the state at which most suction occurred. To further investigate the mechanism behind the observed "suction" phenomenon, the molecular interaction energy was used for the considered pair, which was averaged over the simulation run after the system reached equilibrium to indicate the interaction between the considered pair. The interaction energies between water and K^+-smectite and between water and water and the relationship to changes in pressure were analyzed (Figure 3) for basal spacings of 1.47 nm and 1.66 nm (around ~0.8 and 1.0 nm pore sizes). The interaction energies were in the order of K^+-smectite layer > K^+- water > K^+- K^+. The interaction energies between the smectite layer and the cations (K^+) dominated other interactions when the water content was less than 15 wt.%. The dominant effect of the K^+-smectite layer interaction became less significant as the water content was increased. This was indicated by the less negative values of the K^+- smectite layer interaction energies at higher water contents because the less negative values signified weaker interactions. Once the

water contents reached values larger than 15 wt.%, the water-water interactions became dominant.

The interaction energies between water and K^+-smectite and between water and water (Figures 3b and 3c) were compared. A close inspection of the pressure results (Figures 2b and 2c) revealed that the minimum pressures for 1.47 nm and 1.66 nm basal spacings corresponded to a state with maximum absolute values for the second derivatives of the interaction energies between water and K^+-smectite and between water and water (insets in Figures 3b and 3c). Note that K^+ is part of K^+-smectite and the water and K^+-smectite interactions are the sum of the water-smectite layer and water-K^+ interactions. Notice also that the slopes in Figures 3b and 3c changed. The rate of change in a slope is determined by the second derivative (insets in Figures 3b and 3c) of the interaction energy with respect to the water content. For both the 1.47 nm and 1.66 nm basal spacings, the interaction energies between water and K^+-smectite (Figures 3b and 3c) have a negative second derivative, which is consistent with the downward concavity. Thus, the slope of the curves decreased as
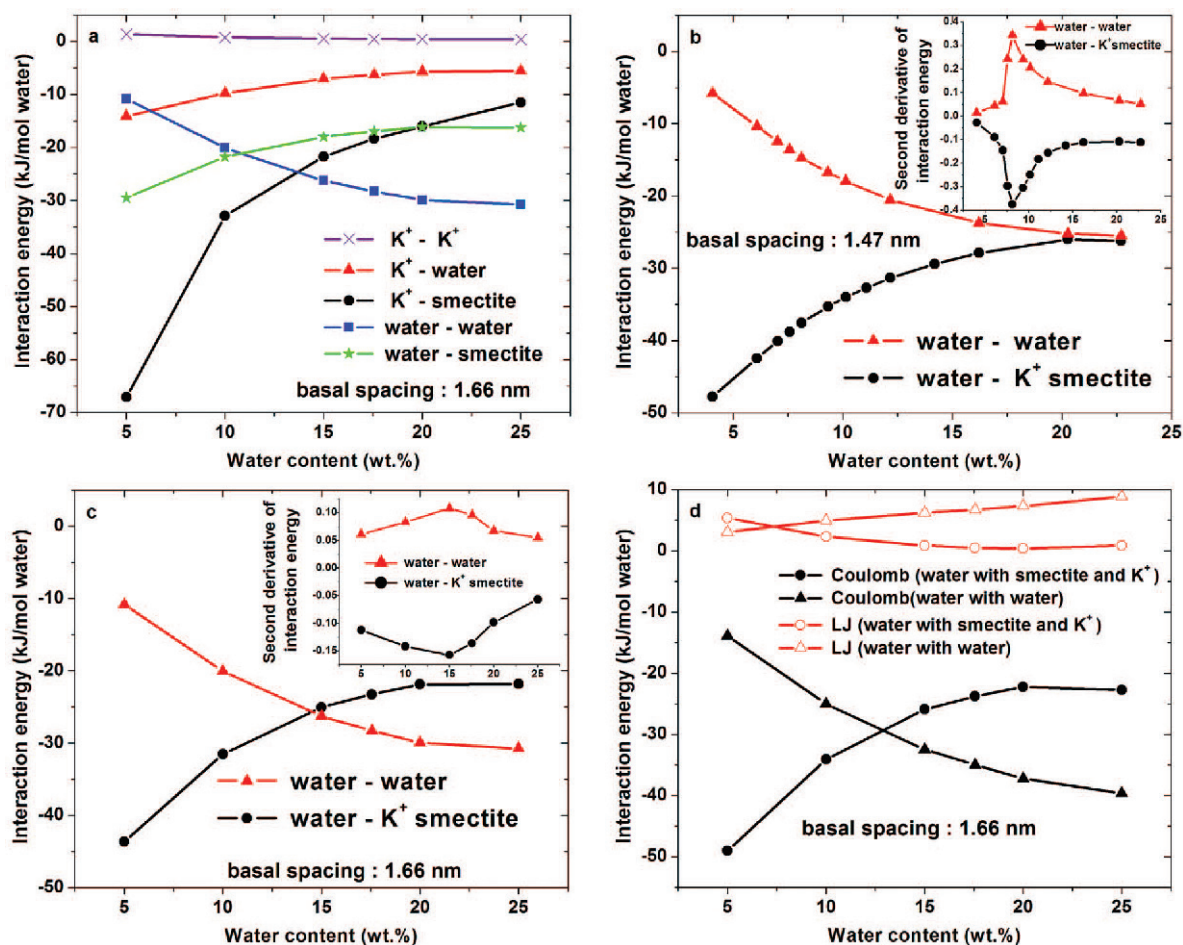
Figure 3. (a) Interaction energies of K^+-smectite, K^+-water, K^+-K^+, water-water, and water-smectite for a basal spacing of 1.66 nm (interlayer pore size of 1 nm); (b) interaction energies of water with K^+-smectite and water with water for a basal spacing of 1.47 nm (interlayer pore size of ~0.8 nm). The inset is the second derivative of the interaction energies with respect to the water contents; (c) interaction energies of water with K^+-smectite and water with water for a basal spacing of 1.66 nm (interlayer pore size of ~1 nm). The inset is the second derivative of the interaction energy with respect to the water content; (d) contributions to the interaction energy from the Coulomb and LJ interactions of water with water and water with K^+-smectite for a basal spacing of 1.66 nm (interlayer pore size of ~1 nm).

the water content was increased. The magnitude of the second derivative of the water and K^+-smectite interaction energy reached a maximum (most negative value) for about 10 wt.% and 15 wt.% water contents for the 1.47 nm and 1.66 nm basal spacings, respectively. The interaction energies between water and water, however, had a positive second derivative (insets in Figures 3b and 3c) suggested by the concave up curves, which indicate that the slopes increased as the water content increased. The maximum second derivative of the water-water interaction energy took place at the same water content as the maximum second derivative of the water and K^+-smectite interaction energy. The maximum rate of change in the interaction energy curve slopes corresponded to the minimum pressure (Figures 2b and 2c).

To further investigate contributions to the interaction energy from the Coulombic and the LJ interactions between water and K^+-smectite and between water and

water, the results for the 1.66 nm basal spacing (Figure 3d) revealed that the Coulombic interaction dominated over the LJ interaction, especially for water and K^+-smectite when the water content was <~13 wt.%. The dominance of the Coulombic interaction decreased when the water content was increased and indicated that greater water contents reduced the interaction energy between water and K^+-smectite. The Coulombic interactions contributed from the partial charges on the atoms of each water molecule became more significant as the water content was increased. This was confirmed by the Coulombic interaction energies between water and water (Figure 3d). Pellenq *et al.* (1997) performed (NVT) Monte Carlo simulations to study the stability of two parallel charged surfaces (lamellae) neutralized by exchangeable counter ions and showed that the behavior of the system was governed by a competition between repulsive forces and attractive forces. The present work

showed that the system behavior was controlled primarily by an interplay between the water with K^+-smectite and water with water interactions (Figures 3b and 3c). Pelleng *et al.* (1997) and the present work show the effect of the interaction forces on the system behavior.

Elasticity stiffness tensor

For each hydration state, the method introduced in the *Simulation details* section was used to obtain the elastic constant of K^+-smectite with the CLAYFF force field using the GULP program package (Gale, 1997). For the smectite layer structure with a transversely isotropic (TI) symmetry (the symmetry axis is along the *z*-axis or *c* crystallographic axis), the elasticity tensor has the following form:

$$\begin{bmatrix} C_{11} & C_{12} & C_{13} & 0 & 0 & 0 \\ C_{21} & C_{22} & C_{23} & 0 & 0 & 0 \\ C_{31} & C_{32} & C_{33} & 0 & 0 & 0 \\ 0 & 0 & 0 & C_{44} & 0 & 0 \\ 0 & 0 & 0 & 0 & C_{55} & 0 \\ 0 & 0 & 0 & 0 & 0 & C_{66} \end{bmatrix}$$

where, $C_{66} = (C_{11}-C_{12})/2$. The elasticity stiffness matrix has 5 independent constants ($C_{11} = C_{22}$ and $C_{44} = C_{55}$), which are related to the well-known engineering elastic moduli. Direction 3 is the one normal to the clay layers (Z) (*c* crystallographic axis) and directions 1 and 2 in the plane (*a* and *b* crystallographic axes) of the clay layer (XY). Due to TI symmetry, $C_{23} = C_{13}$ and $C_{32} = C_{31}$.

To test the reliability of the computed elastic constants, the results were compared with that of an ideal TI symmetry (Figure 4). The comparison between C_{11} and C_{22} and between C_{66} and $(C_{11}-C_{12})/2$ showed that they were not strictly equal, but reasonably close as the difference between C_{11} and C_{22} was within 8%. The C_{66} and $(C_{11}-C_{12})/2$ values were found to differ by less than 3%. Off-diagonal values (except C_{12}, C_{13}, C_{21}, C_{23}, C_{31}, C_{32}) were not zero, but were smaller than C_{11}, C_{12}, C_{22}, and C_{66}.
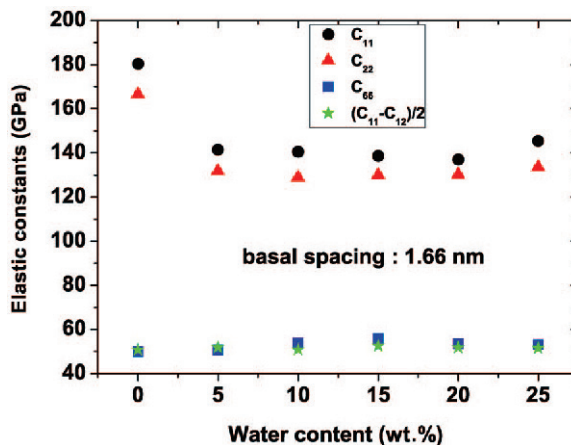

Figure 4. Comparison between C_{11} and C_{22} and between C_{66} and $(C_{11} - C_{12})/2$ for the dry K^+-smectite with a basal spacing of 1.66 nm to test the computed results against that of an ideal TI symmetry.

The C_{11}, C_{22}, and C_{66} values calculated for the dry K^+-smectite with a basal spacing of 1.66 nm in the present study were compared to values calculated by Hantal *et al.* (2014) and Militzer *et al.* (2011) (Table 1) for illite. The C_{11}, C_{22}, and C_{66} values calculated for K+-smectite in the present study were close to those calculated by Militzer *et al.* (2011) for illite. Voigt bulk modulus, Voigt shear modulus, and the speed of sound (V_S and V_P) values were comparable to the values reported by Hantal *et al.* (2014). The calculated C_{33}, C_{44}, and C_{13} values were, however, lower than the Militzer *et al.* (2011) and Hantal *et al.* (2014) values. The in-plane stiffness parameters (C_{11}, C_{12}, C_{22}, and C_{66}) calculated by Hantal *et al.* (2014) were larger than the values in the present work by about 62% to 80% and were higher than the Militzer *et al.* (2011) values by about 45% to 411%. This large difference might have been caused by the different simulation methods that were used.

The Hantal *et al.* (2014) in-plane stiffness parameters were about 40−80% higher than the Sato *et al.* (2005)

Table 1. Comparison of the elastic properties and the P-wave and S-wave velocities from the simulation results for a dry K^+-smectite with a basal spacing of 1.66 nm to published values from Militzer *et al.* (2011) and Hantal *et al.* (2014).

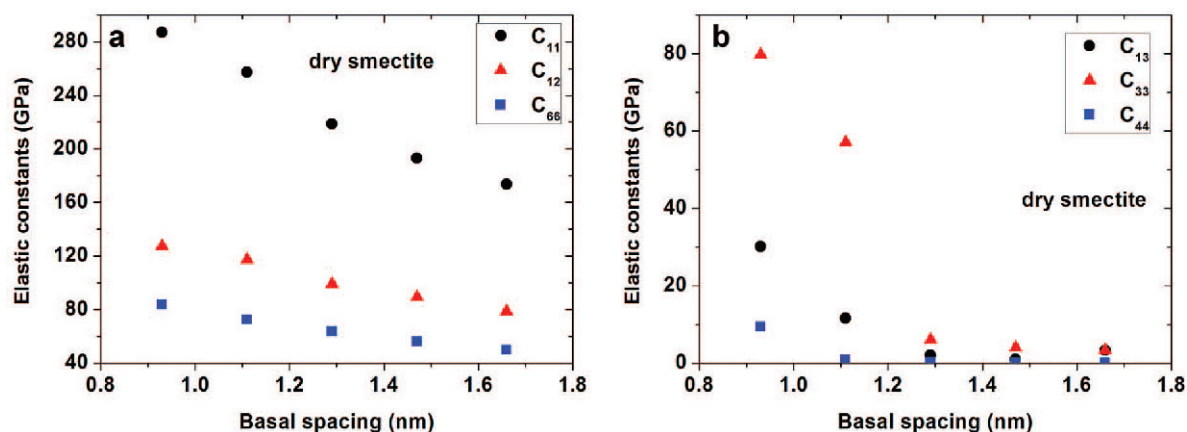| Elastic properties	This work (dry smectite)	Militzer *et al.* (2011)	Hantal *et al.* (2014)
C_{11}/GPa	180.5	153.9	292
C_{22}/GPa	166.6	188.5	274
C_{33}/GPa	4.4	27.2	48.9
C_{44}/GPa	0.1	10.4	9.0
C_{55}/GPa	49.9	55.4	90.1
C_{12}/GPa	78.8	25.1	128.3
C_{13}/GPa	3.6	13.2	16.7
Bulk modulus/GPa	55.9		73.7
Shear modulus/GPa	28.5		35.1
Velocity, V_S /km/s	4.1		3.5
Velocity, V_P /km/s	7.5		6.5

Figure 5. Effect of the smectite layer spacing on (a) the in-plane elastic constant; (b) out-of-plane elastic constant.

values. The C_{11} and C_{12} simulation results in the present study were around 1.4% and 10.9% higher than the corresponding Sato *et al*. (2015) values, while the C_{22} and C_{66} values were around 16% lower.

The elastic coefficient in the transverse direction C_{33} from the simulation on dry K^+-smectite with a basal spacing of 1.66 nm (interlayer pore size of around 1 nm) was substantially lower than the Hantal *et al*. (2014) and Militzer *et al*. (2011) values. This suggests that density and interlayer binding might have been underestimated. Militzer *et al*. (2011) reported illite-smectite densities of 2.6−2.923 g/cm³ (obtained by different methods), which corresponds to a basal spacing of 1.05−0.93 nm in the clay interlayer in the present work. Militzer *et al*. (2011) concluded that the 27.2 GPa C_{33} value, obtained from the local density approximation (LDA) calculations, was their most accurate to predict illite-smectite elastic properties. The LDA density of 2.825 g/cm³ corresponds to a basal spacing of 0.964 nm. Not surprisingly, the C_{33} value from the simulation in the present study was lower than their predicted value because the 1.66 nm smectite basal spacing used in the present study was larger than 0.964 nm value used by Militzer *et al*. (2011) and was selected because the purpose of the present study was to investigate the effects of different water contents (0−25 wt.%) on the elastic properties and a larger pore space was needed to allow room for water molecules.

The simulations of the in-plane (Figure 5a) and out-of-plane (Figure 5b) elastic constants indicated that an increased layer spacing led to a decrease in both the in-plane and out-of-plane elastic constants. The in-plane elastic constant was more linearly related to the basal spacing than the out-of-plane elastic constant. With basal spacings >1.11 nm, the value of the out-of-plane elastic constant dropped significantly. This could be explained by the fact that an increased basal spacing led to an increase in the average distance between atoms and, therefore, the force between two atoms and the derivative of the force with respect to the distance between atoms decreased. The simulations of the out-of-

plane stiffness (Figure 5b) varied significantly from the small 0.93−1.11 nm basal spacings to the larger 1.29−1.66 nm basal spacings.

The full elastic stiffness (in-plane and out-of-plane stiffness) values of K^+-smectite with a basal spacing of 1.66 nm and various water contents (0−25 wt.%) were investigated (Figure 6). The elasticity in the in-plane and in the transverse direction were indeed very different. The elasticity in the in-plane direction was in general larger than in the transverse direction. The smectite layer exhibited a crystalline structure. The displacement of each atom within the layer was very small even when a large force was applied. The in-plane stiffness was, therefore, larger. In contrast, in the transverse direction the interactions responsible for cohesion were the combined effects of the interactions of K^+-smectite layer, K^+ - water, K^+ - K^+, water - water, and water - smectite layer. Close inspection of the normal pressure (Figure 2) and elastic constants (Figure 6) revealed that the various trends in the four in-plane stiffness parameters correlated to variations in the normal pressure changes due to water. The in-plane stiffness was sensitive to normal pressure variations as a result of
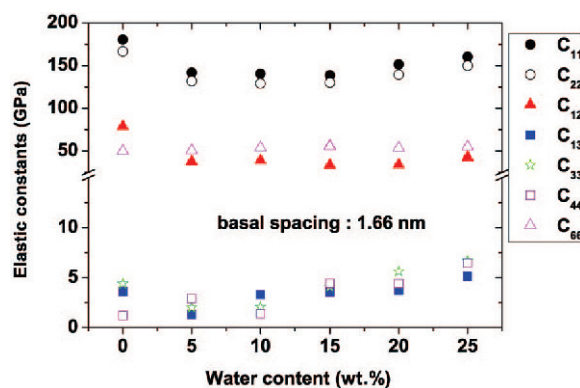

Figure 6. Full elastic stiffness (in-plane and out-of-plane) for a basal spacing of 1.66 nm (pore size of ~1 nm) and various water contents of 0−25 wt.%.

the interplay of the interactions instead of the water content.

Isotropic elastic moduli

The Voigt average for the bulk modulus of hexagonal systems is well known as:

$$K = [2(C_{11} + C_{12}) + 4C_{13} + C_{33}]/9 \quad (5)$$

Similarly, the shear modulus was calculated using:

$$\mu = 1/5[(C_{11} + C_{33} - 2C_{13} - C_{66})/3 + 2C_{44} + 2C_{66} \quad (6)$$

Equations 5 and 6 were used to estimate the bulk and shear moduli from the computed elastic constants. The K and μ values were independently calculated from the C_{ij} values. This approach was not completely rigorous, but provided a reasonable estimate of the elastic properties of a macroscopic isotropic solid.

Voigt bulk and shear moduli computed using CLAYFF force field as introduced in the *Simulation details* section showed the effects of water content (0−25 wt.%) (Figure 7a) on the moduli for K⁺-smectite with a basal spacing of 1.66 nm (interlayer pore size of 1 nm) and the effect of the basal spacing (0.93 nm−1.66 nm) or pore size (0.27 nm−1 nm) (Figure 7b) on the moduli for dry smectite. The moduli correlated with the normal pressure variations (Figure 2) as did the elastic constants (Figure 6). The bulk modulus is known as the incompressibility of the medium. If the bulk modulus was very large, the medium was very stiff, which means that it did not compress very much even under a large force. The shear modulus describes the difficulty with which the medium deforms under an applied shearing force. The moduli results (Figure 7) showed that the values of the Voigt bulk modulus were much higher than the shear modulus. The calculated Voigt bulk and shear moduli for dry K⁺-smectite with a basal spacing of 1.66 nm (bulk: 55.9 GPa; shear: 30.8 GPa) (Figure 7a) were lower than the results (bulk: 73.7 GPa; shear: 35.2 GPa) of Hantal *et*

al. (2014) for illite. The difference could be caused by different isomorphic cation substitutions in the clay layers. The charge of smectite layers varies between -0.4 *e* and −1.2 *e* per unit cell depending on the number of isomorphic cation substitutions. A unit cell layer charge of −1 e was used in the present study, while Hantal *et al.* (2014) used a −1.5 *e* layer charge. The layer charge affects the number of the counter balancing cations (K⁺). As demonstrated in Figure 3, the K⁺-smectite interaction dominated, especially in a dry state or at low water contents and the interaction controlled the behavior of the normal pressure change (Figure 2).

The smectite results were also compared with montmorillonite calculations by Carrier *et al.* (2014). The shear moduli values of 27−31 GPa in the present study were in good agreement with the 12−30 GPa values of Carrier *et al.* (2014) for an isotropic, polycrystalline montmorillonite at 300 K with Na or Ca interlayer cations. The shear moduli values were also comparable to the 16.4−20.3 GPa values for two Na-rich montmorillonites, the 17.1−24.4 GPa values for two Ca-rich montmorillonites, the 18.4 GPa values for illite - smectite mixed layer, and the 25.3 GPa values for illite reported by Wang *et al.* (2001). The bulk moduli for dry K⁺-smectite with a basal spacing of 1.66 nm were in the range of 38.9−55.9 GPa. As in the Carrier *et al.* (2014) study, the dry state bulk moduli were higher than the wet state moduli. Wang *et al.* (2001) measured 29.7−34.7 GPa values for two Na-rich montmorillonites, 37.8−49.6 GPa for two Ca-rich montmorillonites, 36.7 GPa for illite - smectite mixed layer, and 60.1 GPa for illite. The order of magnitude of the K-smectite bulk moduli values in the present study were the same as those measured by Wang *et al.* (2001).

Velocity of P-waves and S-waves

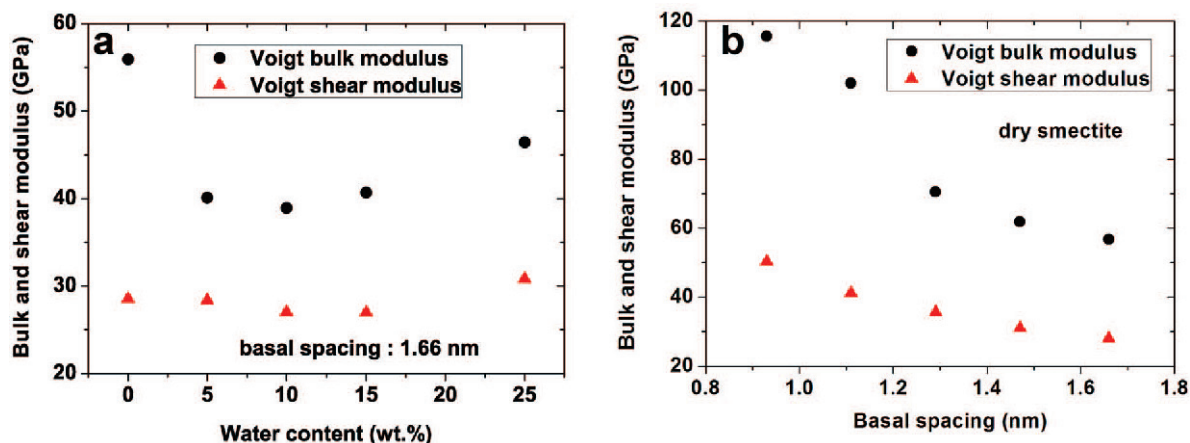The velocity of P-waves in a homogeneous isotropic medium is given by:

Figure 7. Voigt bulk and shear moduli. (a) Water effect on the moduli of K⁺-smectite with a basal spacing of 1.66 nm (interlayer pore size of ~1 nm); (b) basal spacing or pore size effect on the moduli of dry smectite.

$$V_p = \sqrt{\frac{K + 4\mu/3}{\rho}} \qquad (7)$$

and the velocity of S-waves is defined by:

$$V_s = \sqrt{\frac{\mu}{\rho}} \qquad (8)$$

where K is the bulk modulus, μ is the shear modulus, and ρ is the density of the material through which the wave propagates. The speed of P-waves in solids is determined by the bulk modulus, shear modulus, and density. The speed of S-waves is determined only by the solid material shear modulus and density.

The velocities of P-waves and S-waves (Figure 8) indicate the effect of water contents (0−25 wt.%) for K^+-smectite with a basal spacing of 1.66 nm (Figure 8a) and the effect of the basal spacing (0.93−1.66 nm) or pore size (0.27−1 nm) on the velocities in dry smectite (Figure 8b). The velocities decreased with increased water contents due to the density increase from a given fixed volume. The elastic property values reported by Hantal *et al*. (2014) (Table 1) were compared to values determined in the present study and revealed that their 6.5 km/s V_P and 3.5 km/s V_S values were around 14% lower than the corresponding 7.1 km/s and 4.1 km/s values determined in the present study for the dry state. The difference might be attributed to the difference in density and basal spacing.

CONCLUSIONS

The elastic properties of a typical clay mineral, smectite, were investigated by performing combined MD and GULP simulations on dry and moist smectites at fixed basal spacings of ~0.93 to 1.66 nm (interlayer pore size of ~0.27 to 1 nm) and a temperature of 353 K. The

CLAYFF force field for both MD and GULP was used to accurately produce the elastic properties of dry and hydrated smectite mineral systems. Various mechanical properties were determined in terms of pressure, elastic constants, bulk modulus, shear modulus, and the S- and P-wave velocities of K^+-smectite with various water contents and basal spacings. The results were compared to a general ideal layered material with TI symmetry and also compared to previously simulated or experimentally measured values for the same clay mineral (smectite), or other clay minerals like illite - smectite

The results of the pressure and interaction energies between water and K^+-smectite and between water and water indicated that the maximum suction corresponded to the maximum rate of slope change for the interaction energies between water and K^+-smectite and between water and water (the maximum absolute value of the second derivative of the interaction energies with respect to the water content).

The in-plane stiffness parameters (C_{11}, C_{22}, C_{12}, and C_{66}) were more correlated with pressure changes in the presence of water than with the water contents. The calculated in-plane stiffness parameters were comparable to other simulations using different methods. The out-of-plane coefficients (C_{13}, C_{33}, C_{44}, and C_{55}) varied significantly from the simulation results of the different referenced studies. The differences might be caused by the differences in the interlayer cations, isomorphic substitutions, and basal spacings. Moreover, the S- and P-wave velocities were also evaluated.

From a microscopic perspective, the elastic properties of the clay matrix or particles were offered. This study provides a quantitative understanding of the effects of water and pore size on elastic properties from a microscopic perspective. At the macroscopic level, the clay minerals are composed of aggregated clay particles with different pore sizes. Therefore, the elastic properties of clay particles from microscopic simulations might
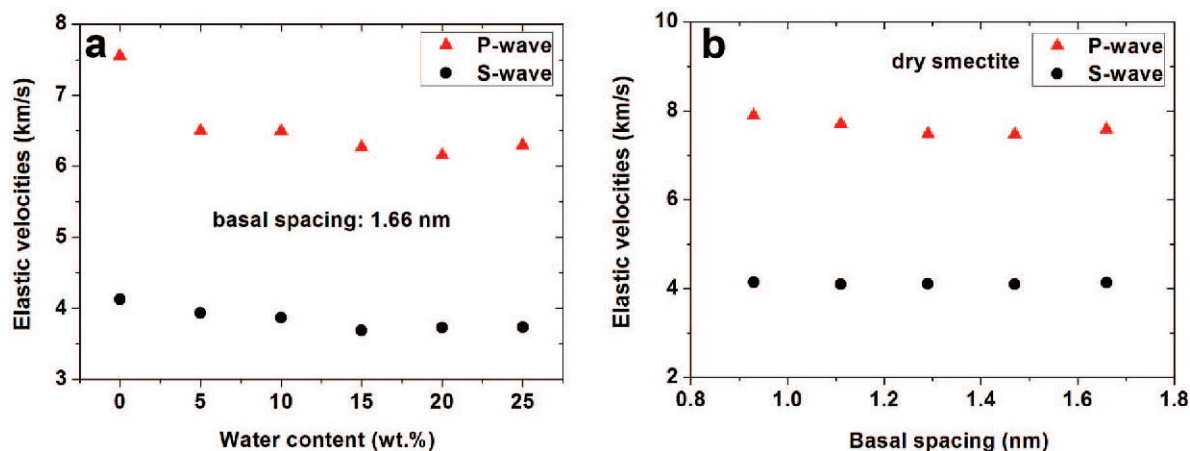

Figure 8. Velocities of P-waves and S-waves. (a) Water effect on the velocities for K^+-smectite with a basal spacing of 1.66 nm (interlayer pore size of ~1 nm); (b) basal spacing or pore size effect on the velocities for dry smectite.

overestimate the properties of actual clay materials, which not only contain particles but also contain the voids formed between particles.

ACKNOWLEDGMENTS

REFERENCES

Bailey, S.W. (1980) Structures of layer silicates, Chapter 1, p. 5 in: *Crystal Structures of Clay Minerals and Their X-ray Identification* (G.W. Brindley and G. Brown, editors). Mineralogical Society, London.

Bayuk, I.O., Ammerman, M., and Chesnokov, E.M. (2007) Elastic moduli of anisotropic clay. *Geophysics*, **72**, D107−D117.

Benazzouz, B.K. and Zaoui, A. (2012) A nanoscale simulation study of the elastic behaviour in kaolinite clay under pressure. *Materials Chemistry and Physics*, **132**, 880−888.

Berendsen, H.J.C., Grigera, J.R., and Straatsma, T.P. (1987) The missing term in effective pair potentials. *Journal of Physical Chemistry*, **91**, 6269−6271.

Berendsen, H.J.C., Postma, J.P.M., Vangunsteren, W.F., Dinola, A., and Haak, J.R. (1984) Molecular-dynamics with coupling to an external bath. *Journal of Chemical Physics*, **81**, 3684−3690.

Boek, E.S., Coveney, P.V., and Skipper, N.T. (1995) Monte Carlo molecular modeling studies of hydrated Li-, Na-, and K-smectites: Understanding the role of potassium as a clay swelling inhibitor. *Journal of the American Chemical Society*, **117**, 12608−12617.

Brindley, G.W. (1980) Order-disorder in clay mineral structures, Chapter 2, p. 170 in: *Crystal Structures of Clay Minerals and Their X-ray Identification* (G.W. Brindley and G. Brown, editors). Mineralogical Society, London.

Carcione, J.M. (2000) A model for seismic velocity and attenuation in petroleum source rocks. *Geophysics*, **65**, 1080−1092.

Carpenter, B.M., Kitajima, H., Sutherland, R., Townend, J., Toy, V.G., and Saffer, D.M. (2014) Hydraulic and acoustic properties of the active Alpine Fault, New Zealand: Laboratory measurements on DFDP-1 drill core. *Earth and Planetary Science Letters*, **390**, 45−51.

Carrier, B., Vandamme, M., Pellenq, R.J.M., and Van Damme, H. (2014) Elastic properties of swelling clay particles at finite temperature upon hydration. *Journal of Physical Chemistry C*, **118**, 8933−8943.

Chalmers, G.R.L. and Bustin, R.M. (2008) Lower Cretaceous gas shales in northeastern British Columbia, Part I: Geological controls on methane sorption capacity. *Bulletin of Canadian Petroleum Geology*, **56**, 1−21.

Chen, G., Zhang, J., Lu, S., Pervukhina, M., Liu, K., Xue, Q., Tian, H., Tian, S., Li, J., Clennell, M.B., and Dewhurst, D.N. (2016) Adsorption behavior of hydrocarbon on illite. *Energy & Fuels*, **30**, 9114−9121.

Chesnokov, E.M., Tiwary, D.K., Bayuk, I.O., Sparkman, M.A., and Brown, R.L. (2009) Mathematical modelling of anisotropy of illite-rich shale. *Geophysical Journal International*, **178**, 1625−1648.

Cook, J.E., Goodwin, L.B., Boutt, D.F., and Tobin, H.J. (2015) The effect of systematic diagenetic changes on the mechanical behavior of a quartz-cemented sandstone. *Geophysics*,

80, D145−D160.

Cygan, R.T., Liang, J.J., and Kalinichev, A.G. (2004) Molecular models of hydroxide, oxyhydroxide, and clay phases and the development of a general force field. *Journal of Physical Chemistry B*, **108**, 1255−1266.

Ebrahimi, D., Pellenq, R.J.M., and Whittle, A.J. (2012) Nanoscale elastic properties of montmorillonite upon water adsorption. *Langmuir*, **28**, 16855−16863.

Ebrahimi, D., Whittle, A.J., and Pellenq, R.J.M. (2016) Effect of polydispersity of clay platelets on the aggregation and mechanical properties of clay at the mesoscale. *Clays and Clay Minerals*, **64**, 425−437.

El Husseiny, A. and Vanorio, T. (2015) The effect of micrite content on the acoustic velocity of carbonate rocks. *Geophysics*, **80**, L45−L55.

Escamilla-Roa, E., Nieto, F., and Sainz-Diaz, C.I. (2016) Stability of the hydronium cation in the structure of illite. *Clays and Clay Minerals*, **64**, 413−424.

Essmann, U., Perera, L., Berkowitz, M. L., Darden, T., Lee, H., and Pedersen, L. G. (1995) A smooth particle mesh Ewald method. *Journal of Chemical Physics.* **103**, 8577 − 8593.

Ferrage, E. (2016) Investigation of the interlayer organization of water and ions in smectite from the combined use of diffraction experiments and molecular simulations. A review of methodology, applications, and perspectives. *Clays and Clay Minerals*, **64**, 348−373.

Gale, J.D. (1997) Gulp: A computer program for the symmetry-adapted simulation of solids. *Journal of the Chemical Society-Faraday Transactions*, **93**, 629−637.

Gualtieri, A.F., Ferrari, S., Leoni, M., Grathoff, G., Hugo, R., Shatnawi, M., Paglia, G., and Billinge, S. (2008) Structural characterization of the clay mineral illite-1M. *Journal of Applied Crystallography*, **41**, 402−415.

Hantal, G., Brochard, L., Laubie, H., Ebrahimi, D., Pellenq, R.J.M., Ulm, F.J., and Coasne, B. (2014) Atomic-scale modelling of elastic and failure properties of clays. *Molecular Physics*, **112**, 1294−1305.

Horn, R.G. (1990) Surface forces and their action in ceramic materials. *Journal of the American Ceramic Society*, **73**, 1117−1135.

Hornby, B.E., Schwartz, L.M., and Hudson, J.A. (1994) Anisotropic effective-medium modeling of the elastic properties of shales. *Geophysics*, **59**, 1570−1583.

Hulan, T., Kaljuvee, T., Stubna, I., and Trnik, A. (2016) Investigation of elastic and inelastic properties of Estonian clay from a locality in Kunda during thermal treatment. *Journal of Thermal Analysis and Calorimetry*, **124**, 1153−1159.

Hulan, T., Trnik, A., Stubna, I., Bacik, P., Kaljuvee, T., and Vozar, L. (2015) Development of Young's modulus of illitic clay during heating up to 1100 degrees C. *Materials Science-Medziagotyra*, **21**, 429−434.

Jankula, M., Hulan, T., Stubna, I., Ondruska, J., Podoba, R., Sin, P., Bacik, P., and Trnik, A. (2015) The influence of heat on elastic properties of illitic clay Radobica. *Journal of the Ceramic Society of Japan*, **123**, 874−879.

Jeppson, T.N. and Tobin, H.J. (2015) San Andreas fault zone velocity structure at SAFOD at core, log, and seismic scales. *Journal of Geophysical Research-Solid Earth*, **120**, 4983−4997.

Kalinichev, A.G., Liu, X.D., and Cygan, R.T. (2016) Introduction to a special issue on molecular computer simulations of clays and clay-water interfaces: Recent progress, challenges, and opportunities. *Clays and Clay Minerals*, **64**, 335−336.

Khazanehdari, J. and McCann, C. (2005) Acoustic and petrophysical relationships in low-shale sandstone reservoir rocks. *Geophysical Prospecting*, **53**, 447−461.

Kitamura, K., Takahashi, M., Mizoguchi, K., Masuda, K., Ito,

H., and Song, S.R. (2010) Effects of pressure on pore characteristics and permeability of porous rocks as estimated from seismic wave velocities in cores from TCDP Hole-A. *Geophysical Journal International*, **182**, 1148−1160.

Kleipool, L.M., Reijmer, J.J.G., Badenas, B., and Aurell, M. (2015) Variations in petrophysical properties along a mixed siliciclastic carbonate ramp (Upper Jurassic, Ricla, NE Spain). *Marine and Petroleum Geology*, **68**, 158−177.

Knuth, M.W., Tobin, H.J., and Marone, C. (2013) Evolution of ultrasonic velocity and dynamic elastic moduli with shear strain in granular layers. *Granular Matter*, **15**, 499−515.

Lein, A.Y., Pimenov, N.V., Savvichev, A.S., Pavlova, G.A., Vogt, P.R., Bogdanov, Y.A., Sagalevich, A.M., and Ivanov, M.V. (2000) Methane as a source of organic matter and carbon dioxide of carbonates at a cold seep in the Norway Sea. *Geochemistry International*, **38**, 232−245.

Liu, D., Yuan, P., Liu, H.M., Li, T., Tan, D.Y., Yuan, W.W., and He, H.P. (2013) High-pressure adsorption of methane on montmorillonite, kaolinite and illite. *Applied Clay Science*, **85**, 25−30.

Mazo, M.A., Manevitch, L.I., Gusarova, E.B., Berlin, A.A., Balabaev, N.K., and Rutledge, G.C. (2008) Molecular dynamics simulation of thermomechanical properties of montmorillonite crystal. II. Hydrated montmorillonite crystal. *Journal of Physical Chemistry C*, **112**, 17056−17062.

Militzer, B., Wenk, H.R., Stackhouse, S., and Stixrude, L. (2011) First-principles calculation of the elastic moduli of sheet silicates and their application to shale anisotropy. *American Mineralogist*, **96**, 125−137.

Pellenq, R.J.M., Caillol, J.M., and Delville, A. (1997) Electrostatic attraction between two charged surfaces: A (N,V,T) Monte Carlo simulation. *Journal of Physical Chemistry B*, **101**, 8584−8594.

Prasad, M., Kopycinska, M., Rabe, U., and Arnold, W. (2002) Measurement of Young's modulus of clay minerals using atomic force acoustic microscopy. *Geophysical Research Letters*, **29**, 13-1−13-4.

Renner, K., Henning, S., Moczo, J., Yang, M.S., Choi, H.J., and Pukanszky, B. (2007) Micromechanical deformation processes in PA/layered silicate nanocomposites: Correlation of structure and properties. *Polymer Engineering and Science*, **47**, 1235−1245.

Ross, D.J.K. and Bustin, R.M. (2009) The importance of shale composition and pore structure upon gas storage potential of shale gas reservoirs. *Marine and Petroleum Geology*, **26**, 916-927.

Sainz-Diaz, C.I., Hernandez-Laguna, A., and Dove, M.T. (2001) Theoretical modelling of *cis*-vacant and *trans*-vacant configurations in the octahedral sheet of illites and smectites. *Physics and Chemistry of Minerals*, **28**, 322−331.

Sainz-Diaz, C.I., Palin, E.J., Dove, M.T., and Hernandez-Laguna, A. (2003) Monte Carlo simulations of ordering of Al, Fe, and Mg cations in the octahedral sheet of smectites and illites. *American Mineralogist*, **88**, 1033−1045.

Sarout, J., Esteban, L., Delle Piane, C., Maney, B., and Dewhurst, D.N. (2014) Elastic anisotropy of Opalinus Clay under variable saturation and triaxial stress. *Geophysical Journal International*, **198**, 1662−1682.

Sato, H., Ono, K., Johnston, C.T., and Yamagishi, A. (2005) First-principles studies on the elastic constants of a 1:1 layered kaolinite mineral. *American Mineralogist*, **90**, 1824−1826.

Schon, J.H., Georgi, D.T., and Tang, X.M. (2006) Elastic wave anisotropy and shale distribution. *Petrophysics*, **47**, 239−249.

Schumann, K., Stipp, M., Behrmann, J.H., Klaeschen, D., and Schulte-Kortnack, D. (2014) *P* and *S* wave velocity measurements of water-rich sediments from the Nankai Trough, Japan. *Journal of Geophysical Research-Solid Earth*, **119**, 787−805.

Skipper, N.T., Refson, K., and Mcconnell, J.D.C. (1991a) Computer simulation of interlayer water in 2:1 clays. *Journal of Chemical Physics*, **94**, 7434−7445.

Skipper, N.T., Soper, A.K., and Mcconnell, J.D.C. (1991b) The structure of interlayer water in vermiculite. *Journal of Chemical Physics*, **94**, 5751−5760.

Smith, D.E. (1998) Molecular computer simulations of the swelling properties and interlayer structure of cesium montmorillonite. *Langmuir*, **14**, 5959−5967.

Van der Spoel, D., Lindahl, E., Hess, B., Groenhof, G., Mark, A.E., and Berendsen, H.J.C. (2005) Gromacs: Fast, flexible, and free. *Journal of Computational Chemistry*, **26**, 1701−1718.

Vanorio, T., Prasad, M., and Nur, A. (2003) Elastic properties of dry clay mineral aggregates, suspensions and sandstones. *Geophysical Journal International*, **155**, 319−326.

Wang, Z., Gelius, L.J., and Kong, F.N. (2009) Simultaneous core sample measurements of elastic properties and resistivity at reservoir conditions employing a modified triaxial cell − a feasibility study. *Geophysical Prospecting*, **57**, 1009−1026.

Wang, Z.J., Wang, H., and Cates, M.E. (2001) Effective elastic properties of solid clays. *Geophysics*, **66**, 428−440.

Wardle, R. and Brindley, G.W. (1972) Crystal-structures of pyrophyllite, 1Ttc, and of its dehydroxylate. *American Mineralogist*, **57**, 732−750.

Wenk, H.R., Lonardelli, I., Franz, H., Nihei, K., and Nakagawa, S. (2007) Preferred orientation and elastic anisotropy of illite-rich shale. *Geophysics*, **72**, E69−E75.

Witteveen, P., Ferrari, A., and Laloui, L. (2013) An experimental and constitutive investigation on the chemo-mechanical behaviour of a clay. *Geotechnique*, **63**, 244−255.

Woodruff, W.F., Revil, A., Prasad, M., and Torres-Verdin, C. (2015) Measurements of elastic and electrical properties of an unconventional organic shale under differential loading. *Geophysics*, **80**, D363−D383.

Young, D.A. and Smith, D.E. (2000) Simulations of clay mineral swelling and hydration: Dependence upon interlayer ion size and charge. *Journal of Physical Chemistry B*, **104**, 9163−9170.

Zhang, J.F., Clennell, M.B., Liu, K.Y., Pervukhina, M., Chen, G.H., and Dewhurst, D.N. (2016) Methane and carbon dioxide adsorption on illite. *Energy and Fuels*, **30**, 10643−10652.

Zhang, W.N., Hu, H.X., Li, X.C., and Fang, Z.M. (2017) Changes in micromechanical properties of Na-montmorillonite caused by CO_2/H_2O sorption. *Computational Materials Science*, **129**, 178−183.

Zhou, J.H., Lu, X.C., and Boek, E.S. (2016) Changes in the interlayer structure and thermodynamics of hydrated montmorillonite under basin conditions: Molecular simulation approaches. *Clays and Clay Minerals*, **64**, 503−511.

Zou, C.N., Yang, Z., Zhu, R.K., Zhang, G.S., Hou, L.H., Wu, S.T., Tao, S.Z., Yuan, X.J., Dong, D.Z., Wang, Y.M., Wang, L., Huang, J.L., and Wang, S.F. (2015) Progress in China's unconventional oil and gas exploration and development and theoretical technologies. *Acta Geologica Sinica-English Edition*, **89**, 938−971.